PHYSICAL REVIEW B **108**, 035425 (2023)

Enhanced thermoelectric properties in phosphorene nanorings

Fatemeh Moghadasi Borojeni,[1] Esmaeil Taghizadeh Sisakht,[1] Farhad Fazileh,[1,*] and F. M. Peeters[2,3]
[1]*Department of Physics, Isfahan University of Technology, Isfahan 84156-83111, Iran*
[2]*HSE University, Moscow 10100, Russia*
[3]*Departamento de Fisica, Universidade Federal do Ceara, 60455-760 Fortaleza, Ceara, Brazil*

(Received 25 January 2023; revised 5 July 2023; accepted 10 July 2023; published 31 July 2023)

Using the tight-binding approach, we calculate the thermoelectric properties of phosphorene nanorings in the absence and presence of a perpendicular magnetic field, and we investigate the effect of symmetrically and asymmetrically positioned leads. Our findings indicate that the symmetry/asymmetry of our designed nanostructures, the geometrical characteristics of the ring, and the magnetic flux are three important factors in controlling their thermoelectric properties. Our results show that when zigzag phosphorene nanoribbons (ZPNRs) are coupled symmetrically/asymmetrically to rectangular rings, a large band gap is induced in the electronic conductance due to the suppression of the contribution of edge states. This gives rise to a remarkable increase in the thermopower response compared to the case of pristine ZPNRs. More intriguingly, we realized that the significantly smaller electronic thermal conductance and the reduced phonon thermal conductance of these phosphorene-based nanostructures result in a remarkable improvement in the figure of merit. Moreover, for asymmetric connection configurations with armchair-edged leads, we found that although the thermopower is almost intact, a remarkable reduction of the electronic and phononic thermal conductance leads to a notable improvement in the figure of merit. Also, our numerical calculations showed that by changing the magnetic flux through the nanoring, a drastic increase in the thermopower is observed near an antiresonance point. We demonstrate the tunability of the thermopower and the possibility to switch on and off the thermoelectric response with magnetic flux. Our results suggest phosphorene nanorings as promising candidate nanostructures for thermoelectric applications.

DOI: 10.1103/PhysRevB.108.035425

I. INTRODUCTION

Designing devices with optimal thermoelectric (TE) properties is highly desirable for future energy harvesting and environmental issues [1]. TE materials occupy a special place for clean energy research, since they directly convert heat into electrical energy and vice versa and can be used as electrical power generators and cooling (heating) devices. The TE efficiency is given by the dimensionless figure of merit $ZT = \frac{S^2\sigma T}{\kappa}$, where S is the Seebeck coefficient (SC) or thermopower, σ and κ are the electrical and thermal conductivities, respectively, and T is the temperature. From this relation we see that a reduction in thermal conductivity (while the electrical conductivity is kept almost the same) leads to a strong improvement of the TE efficiency. One way to accomplish this task is to construct nanostructures of bulk TE materials [2]. Here, the enhanced TE figure of merit ZT is due to phonon scattering with boundaries and quantum confinement effects. The TE efficiency can be further enhanced by making nanorings [3,4] and taking advantage of the Aharonov-Bohm (AB) effect when we apply an external magnetic field, which allows us to tune the magnetoresistance of the system [5–7].

Among nanostructured semiconducting materials, two-dimensional (2D) phosphorene has received a lot of attention recently due to its great transport properties and potential applications [8–15]. This structure consists of a single layer or a few layers of black phosphorus, and it has been successfully fabricated [10,11,14]. From these studies, it is suggested that because of its remarkable electronic, mechanical, and optical properties, it offers great promise for applications in electronic and optoelectronic devices [16–25]. In addition, due to superior thermoelectric characteristics, it is also proposed that phosphorene nanostructures are highly promising for thermoelectric devices, and it could be their key application in the future [26]. Various factors may significantly affect the three parameters that are used to quantify the figure of merit in this structure. For single crystals of bulk black phosphorus, experiments found that the value of SC is about 340 μV/K at room temperature [27]. It was shown that gate-tuning is a successful way to control the TE power coefficient in a thin flake of black phosphorus [28]. These experimental measurements verified that the SC of ion-gated bulk black phosphorus can reach 510 μV/K at 210 K, which may result in a large increase of ZT compared to that of bulk single crystal at room temperature. The puckered structure of monolayer phosphorene has led to anisotropy in its electrical and thermal properties [29]. Theoretical studies showed that this distinct feature gives rise to orthogonal electrical and thermal conductances [30]. This results in a higher σ/κ ratio and thus in a rather large figure of merit $ZT \sim 1$ (at room temperature) along the armchair direction of monolayer phosphorene [30]. Moreover, it is believed

---

[*] fazileh@iut.ac.ir

that the utilization of nanoribbons of such 2D materials is a way to enhance the TE efficiency. Theoretical calculations predicted that using phosphorene nanoribbons (PNRs) as thermoelectric material can lead to improved TE efficiencies [31]. The effect of the edge states on the thermopower in zigzag phosphorene nanoribbons (ZPNRs) was recently investigated [32]. It was shown that by applying a transverse electric field, one can completely push the edge modes into the bulk bands and maximize the bulk energy gap, which results in enhanced thermoelectric power in PNRs [32]. Also, it was found that the passivation of edge phosphorous atoms with hydrogen in both types of nanoribbon edges [31], and even oxidation in phosphorene oxide [33], enhances the thermopower.

These studies confirm that nanoribbon-based structures of monolayer phosphorene are candidates to improve the TE properties and the advent of efficient TE nanodevices. Recent studies reported the production of high-quality PNRs with relatively large and uniform lengths that may renew the interest in the study of thermoelectric properties in nanoribbons and nanostructured systems made of phosphorene [34]. Nanorings made of two-dimensional materials are possible nanostructures that may be used to improve TE efficiency. For example, TE properties of rectangular graphene nanorings have been investigated and were proposed to build tunable TE generators [3,35]. In such systems, the improvement in their TE performance was attributed to the emergence of Fano line shapes or Breit-Wigner line shapes in the transmission coefficient, which depend on the geometrical characteristics of the ring and the applied side-gate voltage [3]. However, despite the numerous works [28–33] on the TE properties of phosphorene and phosphorene nanoribbons, the TE performance of rectangular phosphorene nanorings has remained elusive so far.

In the present work, inspired by the mentioned methods to improve the TE performance in graphene nanorings, we investigate the thermoelectric characteristics of rectangular phosphorene nanorings for both symmetrical and asymmetrical attachment of leads. We investigate the effect of an applied external magnetic field on the TE properties of these rectangular rings, and we show how the thermoelectric coefficients are controllable in our designed systems by a perpendicular magnetic field. Also, we examine the role of ring size and the symmetry of the connection configuration of leads on the TE response of these systems.

II. MODEL AND FORMALISM

The system under study is a rectangular phosphorene nanoring with a symmetric or asymmetric coupling to two leads, as shown in Figs. 1(a) and 1(b). In each configuration, two semi-infinite zigzag- or armchair-edged nanoribbon of phosphorene connect to a nanoring. The geometry of a rectangular quantum ring is determined by the inner and outer sides L_{in}, W_{in}, L_{out}, and W_{out}. In monolayer phosphorene (MLP), each phosphorus atom (P) is covalently bonded to three neighbor phosphorus atoms, and they form a puckered structure as depicted in Figs. 1(c) and 1(d). The lattice constants of MLP are $a = 4.38$ Å and $b = 3.32$ Å. There are four P atoms in the rectangular primitive unit cell of MLP. The generally accepted low-energy tight-binding (TB) Hamiltonian for pristine MLP is given by [36]

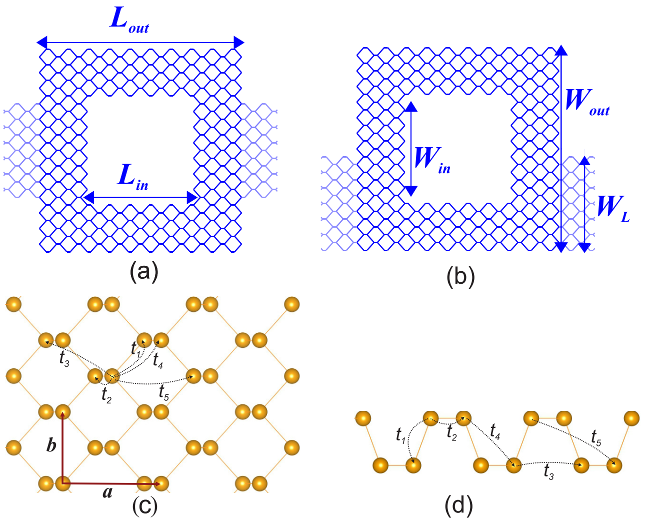

FIG. 1. Parts (a) and (b) show schematically symmetric and asymmetric coupling of a rectangular phosphorene ring to two leads. The geometrical parameters of the system are shown. Parts (c) and (d) show the top view and side view of the lattice structure of monolayer phosphorene, respectively. $\boldsymbol{a}$ and $\boldsymbol{b}$ are lattice vectors. $t_1, \ldots, t_5$ denote the used hopping parameters in our TB model.

$$\mathcal{H}_{\mathrm{MLP}} = \sum_{i \neq j} t_{ij} c_i^{\dagger} c_j, \tag{1}$$

where $c_i^{\dagger}$ (c_i) is the creation (annihilation) operator of an electron at the ith (jth) atom, and t_{ij} are the hopping parameters for different nearest neighbors that run over the five hopping parameters $t_1, \ldots, t_5$ [see Figs. 1(c) and 1(d)]. The specific values of these hopping parameters as suggested in [36] are as follows: $t_1 = -1.220$ eV, $t_2 = 3.665$ eV, $t_3 = -0.205$ eV, $t_4 = -0.105$ eV, and $t_5 = -0.055$ eV.

In our systems of interest [Figs. 1(a) and 1(b)], the bulk of MLP is selectively cut or modified, resulting in the exposure of bare edges or dangling bonds at the surface of the material. The bare edges and geometry of our lead-nanoring-lead configurations can have a significant impact on their electronic and transport properties. Due to the reduced dimensionality in these configurations, their electronic and thermal properties become highly sensitive to the surface or edge structure, which can lead to unique electronic states or enhanced TE properties. Additionally, the geometry of the ring can affect the symmetry of the electronic states and alter the probability of electronic scattering and tunneling, leading to a modification in the transport properties such as conductivity, mobility, and TE response. These bare edges and boundary conditions can be modeled using the TB approximation by imposing certain constraints on the hopping integrals or eliminating the hopping terms involving the edge atoms. This is because the dangling bonds do not have neighboring atoms to which they can hop, and therefore, their contribution to the electronic structure should be ignored. Hence, the whole Hamiltonian of our lead-nanoring-lead system can be written as a sum of four parts: the Hamiltonian of the left (right) lead, the Hamiltonian of the central nanoring device, and the Hamiltonian that describes the coupling between the leads and the device. This Hamiltonian can be written in block matrix form as

$$\mathcal{H} = \begin{pmatrix} \mathcal{H}_{\mathrm{L}} & \mathcal{H}_{\mathrm{LD}} & 0 \\ \mathcal{H}_{\mathrm{LD}}^{\dagger} & \mathcal{H}_{\mathrm{D}} & \mathcal{H}_{\mathrm{DR}} \\ 0 & \mathcal{H}_{\mathrm{DR}}^{\dagger} & \mathcal{H}_{\mathrm{R}} \end{pmatrix}, \tag{2}$$

where $\mathcal{H}_{\mathrm{L}}$ and $\mathcal{H}_{\mathrm{R}}$ are the Hamiltonians of the left and right leads, respectively, $\mathcal{H}_{\mathrm{D}}$ is the Hamiltonian of the central device (nanoring) as scattering region, and $\mathcal{H}_{\mathrm{LD}}$ and $\mathcal{H}_{\mathrm{DR}}$ are the coupling Hamiltonians between the leads and the ring. Note that in our analysis, we assume the size of the ring is sufficiently large to preclude direct hopping between the left and right leads. In the rectangular ring, we label each phosphorus atom with a unique index from 1 to N to specify their position. For the left (right) lead, the lattice sites extend infinitely in one direction and we can label each phosphorous atom with a unique index from $-\infty$ to 0 ($N+1$ to $+\infty$). Therefore, using Eq. (1), the Hamiltonian of the left (right) lead, and the nanoring in the second quantized representation, are given by

$$\mathcal{H}_{\mathrm{L(R)}} = \sum_{i,j=-\infty(N+1)}^{0(+\infty)} t_{ij} c_i^{\dagger} c_j,$$

$$\mathcal{H}_{\mathrm{D}} = \sum_{i,j=1}^{\mathrm{N}} t_{ij} c_i^{\dagger} c_j, \tag{3}$$

respectively, and in each relation $i \neq j$, and $t_{ij} \in t_1, \dots, t_5$. The coupling Hamiltonian between the left (right) lead and nanoring is written as

$$\mathcal{H}_{\mathrm{LD}} = \sum_{k=-\infty}^{0} \sum_{l=1}^{\mathrm{N}} t_{kl} c_k^{\dagger} d_l,$$

$$\mathcal{H}_{\mathrm{DR}} = \sum_{m=1}^{\mathrm{N}} \sum_{n=N+1}^{\infty} t_{mn} d_m^{\dagger} c_n, \tag{4}$$

where $d_m^{\dagger}$ (d_l) is the creation (annihilation) operator for an electron in the nanoring, and $c_k^{\dagger}$ (c_n) is the creation (annihilation) operator for an electron in the left (right) lead. t_{kl} (t_{mn}) represents the hopping integral between site k (m) in the ring and site l (n) in the left (right) lead. The sum runs over all sites in the nanoring and all sites in the leads that are directly coupled to the device.

To evaluate the thermoelectric response of the lead-nanoring-lead system, the transmission coefficient needs to be determined. Various methods can be employed to achieve this, such as utilizing the transfer-matrix technique in the scattering approach [37,38] or utilizing the Fisher-Lee relation associated with the real-space Green's-function method [37]. The S-matrix in a coherent device establishes a relationship between the incoming and outgoing wave amplitudes, allowing us to determine the response of a lead to an excitation originating from another lead. On the other hand, the Green's function is a more versatile tool that enables us to obtain the response at any point, whether inside or outside the conductor, in response to an excitation from any other point. When dealing with noninteracting transport, we only need to account for excitations arising from waves incident from the leads. For such excitations, the Green's function and S-matrix are conceptually similar, and the choice of which to use is primarily a matter of preference [37]. To calculate the conductance of the lead-nanoring-lead system using the S-matrix approach, it is necessary to determine the relationships between incoming and outgoing waves, as well as match the coefficients for these waves in the scattering region. An energy eigenstate $|\psi_E\rangle$ of the lead-nanoring-lead system can be expressed as a linear combination of eigenstates $|\phi^{\pm}_{\mathrm{L},nE}\rangle$ and $|\phi^{\pm}_{\mathrm{R},nE}\rangle$ in the left and right leads, respectively, and by an unknown eigenstate $|\phi_{\mathrm{D},E}\rangle$ in the nanoring. Thus, we can express an eigenstate of the system as

$$|\psi_E\rangle = \begin{cases} \sum_n \left(a^{+}_{\mathrm{L(R)},n} |\phi^{+}_{\mathrm{L(R)},nE}\rangle + a^{-}_{\mathrm{L(R)},n} |\phi^{-}_{\mathrm{L(R)},nE}\rangle\right) & \text{for } \mathrm{L}(R), \\ |\phi_{\mathrm{D},E}\rangle & \text{for ring}, \end{cases} \tag{5}$$

where we have represented the incoming and outgoing wave amplitudes by vectors $\boldsymbol{a}^{+}_{\mathrm{L(R)}} = (a^{+}_{\mathrm{L(R)},1}, a^{+}_{\mathrm{L(R)},2}, \dots)$ and $\boldsymbol{a}^{-}_{\mathrm{L(R)}} = (a^{+}_{\mathrm{L(R)},1}, a^{+}_{\mathrm{L(R)},2}, \dots)$, respectively, and each vector includes all the various modes in the corresponding lead. The outgoing amplitudes can be expressed linearly in terms of the incoming amplitudes by the S-matrix as

$$\begin{pmatrix} \boldsymbol{a}^{-}_{\mathrm{L}} \\ \boldsymbol{a}^{+}_{\mathrm{R}} \end{pmatrix} = \begin{pmatrix} r & \tilde{t} \\ t & \tilde{r} \end{pmatrix} \begin{pmatrix} \boldsymbol{a}^{+}_{\mathrm{L}} \\ \boldsymbol{a}^{-}_{\mathrm{R}} \end{pmatrix}, \tag{6}$$

where r and t are the reflection and transmission matrices in the scattering matrix $S(E)$. In Eqs. (5) and (6), matching the wave functions allows one to determine the coefficients of the incoming and outgoing waves in the scattering region. This shows clearly that the geometry of the leads and the boundary conditions at the interface between the leads and the device region play a crucial role in determining the transport properties of the system. The transmission probability T can be calculated from the S-matrix by taking the modulus squared of the transmission coefficient: $T_{\mathrm{LR}}(E) = \mathrm{tr}\{tt^{*}\}$. So, the two-terminal conductance of charge carriers through a nanoring is given by

$$G = \frac{2e^2}{h} \int \left(-\frac{\partial f_0}{\partial E}\right) T_{\mathrm{LR}}(E)\, dE, \tag{7}$$

where f_0 is the Fermi distribution function $1/[e^{(E-\mu)/K_{\mathrm{B}}T} + 1]$ at temperature T, and $T_{\mathrm{LR}}(E)$ denotes the transmission coefficient of our lead-nanoring-lead system [37,38]. To evaluate the transmission coefficient and local density of states using the Green's-function method, one can derive the retarded (advanced) Green's function of the ring by computing the retarded (advanced) self-energies of the connected leads:

$$G_{\mathrm{D}}^{r(a)} = \left[E^{r(a)} - \mathcal{H}_{\mathrm{D}} - \Sigma_{\mathrm{L}}^{r(a)}(E) - \Sigma_{\mathrm{R}}^{r(a)}(E)\right]^{-1}, \tag{8}$$

where $\Sigma_{\mathrm{L(R)}}(E)$ is the self-energy related to the left (right) lead, and $E^r = E + i\eta$ ($E^a = E - i\eta$). The conductance $\sigma(E)$ of our systems at Fermi energy (E_F) between a pair of leads L and R is given by

$$\sigma(E) = \frac{2e^2}{h} T_{\mathrm{LR}}(E) = \frac{e^2}{h} tr\left[\Gamma_{\mathrm{L}}(E) G_{\mathrm{D}}^{r}(E) \Gamma_{\mathrm{R}}(E) G_{\mathrm{D}}^{a}(E)\right], \tag{9}$$

where $\Gamma_{\mathrm{L(R)}} = i[\Sigma_{\mathrm{L(R)}}(E) - \Sigma^{\dagger}_{\mathrm{L(R)}}(E)]$. Given the retarded Green's function of the central device, it is straightforward to calculate the local density of states (LDOS) at each site i of the central region using the relation [37]

$$\rho_i(E) = -\frac{1}{\pi}\mathrm{Im}G^r_{ii}(E). \tag{10}$$

In the Landauer-Buttiker formalism, the thermopower S and the electronic contribution to thermal conductance κ_e are expressed in terms of the moments of the transmission coefficient [39]

$$K_n = \int_{-\infty}^{\infty}\left(-\frac{\partial f_0}{\partial E}\right)\beta^n(E-\mu)^n T_{\mathrm{LR}}(E)dE, \tag{11}$$

via the following equations:

$$S = -\frac{k_{\mathrm{B}}}{e}\frac{K_1}{K_0}, \tag{12}$$

$$\kappa_e = \frac{2k_{\mathrm{B}}^2 T}{h}\left[K_2 - \frac{K_1^2}{K_0}\right], \tag{13}$$

where $\beta = 1/k_{\mathrm{B}}T$. In the present study, for computational analysis, we employ the PYBINDING code package [40] to construct the tight-binding Hamiltonians for our lead-nanoring-lead device. Subsequently, we evaluate the transport properties using the S-matrix method, which is implemented in the Python package KWANT [41]. Also, we use analytical methods based on Green's functions to elucidate the underlying physics of the observed phenomena.

III. RESULTS

We design our phosphorene-based nanostructures with the aim to enhance the TE performance compared to the TE responses of pristine PNRs. So, before proceeding with our main systems, we first examine the electronic conductance G, the Seebeck coefficient S, the electronic thermal conductance κ_e, and the thermoelectric power factor $\mathrm{PF} = GS^2$ for pristine PNRs. We identify ZPNRs and armchair phosphorene nanoribbons (APNRs) by the number of zigzag chains or dimer lines present across the ribbon's width. They are labeled as N-ZPNR or N-APNR, respectively. In Figs. 2(a) and 3(a), cyan curves show the calculated conductance for typical samples 16-ZPNR ($W = 3.50$ nm) and 20-APNR ($W = 3.32$ nm), respectively. The intriguing electronic properties of ZPNRs and APNRs have a direct consequence on their transport characteristics. The conductance of both ZPNRs and APNRs exhibits quantized plateaus $G = n(2e^2/h)$, where $2e^2/h$ is the conductance quantum and n denotes the number of available transport modes at energy E. As seen, the ZPNR shows a conductance plateau of value $G = 2(2e^2/h)$ near the zero-energy region because of the contribution of edge-propagating states along the zigzag boundaries. On the other hand, due to the absence of propagating edge modes in the APNR, there exists no quantized plateau in the midgap region. Furthermore, the lack of electron-hole symmetry in the electronic band structures of PNRs leads to an asymmetry of their quantum conductance with respect to $\mu = 0$. Figures 2(b) and 3(b) (cyan curves) depict the numerically calculated thermopower S for the ZPNR and APNR, respectively.

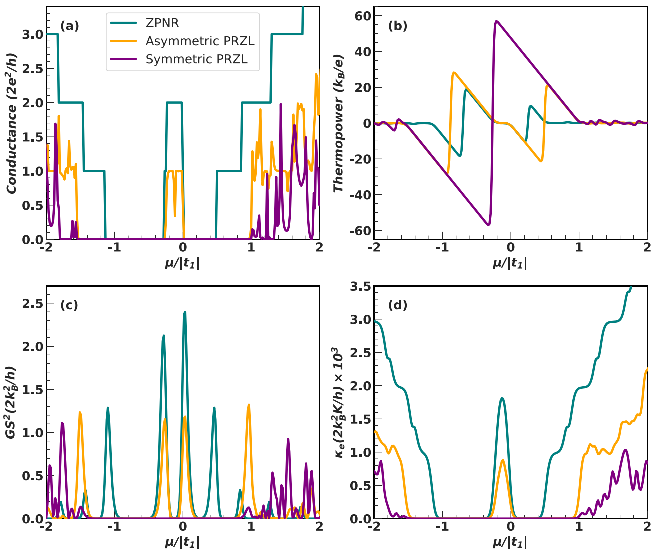

FIG. 2. (a) Electronic conductance, (b) thermopower, (c) power factor, and (d) electronic thermal conductance as a function of scaled chemical potential for 16-ZPNR (cyan curves), an asymmetric PRZL (orange curves), and a symmetric PRZL (purple curves). The structural parameters for PRZLs are set to $W_{\mathrm{in}} = W_{\mathrm{out}}/2 = W_L = 3.5$ nm and $L_{\mathrm{in}} = L_{\mathrm{out}}/2 = 1.66$ nm. The temperature is set to $k_{\mathrm{B}}T = 0.021|t_1|$ in our calculations.

A comparison between the thermopower of the ZPNR and APNR shows that the presence of midgap edge modes drastically affects the SC, and hence is sensitive to the topology of the boundaries in a PNR. We have illustrated in Figs. 2(c) and 3(c) the corresponding power factors, which clearly shows

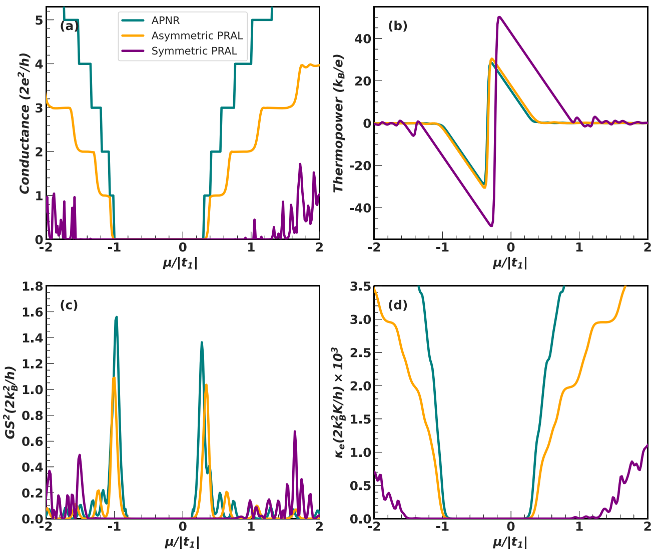

FIG. 3. (a) Electronic conductance, (b) thermopower, (c) power factor, and (d) electronic thermal conductance as a function of scaled chemical potential for 20-APNR (cyan curves), an asymmetric PRAL (orange curves), and a symmetric PRAL (purple curves). The structural parameters for PRALs are set to $W_{\mathrm{in}} = W_{\mathrm{out}}/2 = W_L = 3.32$ nm and $L_{\mathrm{in}} = L_{\mathrm{out}}/2 = 1.75$ nm. The temperature is set to $k_{\mathrm{B}}T = 0.021|t_1|$ in our calculations.

that in the ZPNR case, due to the mentioned edge modes, a maximum power factor appears near the zero Fermi energy. The cyan curves in Figs. 2(d) and 3(d) display the electronic thermal conductance κ_e as a function of the chemical potential μ for ZPNR and APNR, respectively. As seen, due to the lack of electron-hole symmetry, κ_e is also asymmetric around $\mu = 0$.

Now, we investigate the thermoelectric performance of a phosphorene ring with zigzag leads (PRZL). One approach to improve the SC in phosphorene is by creating a substantial band gap in phosphorene nanostructures with zigzag edges, which exhibit metallic characteristics. This can be achieved by connecting two narrow leads of PNR to a rectangular phosphorene nanoring as schematically depicted in Fig. 1. We couple two PNRs with zigzag edges to a rectangular ring for both symmetries. The corresponding results are shown in Figs. 2(a)–2(d) for asymmetric (orange curves) and symmetric (purple curves) configurations. It is found that for a symmetric connection configuration, the conductance and thermopower are considerably affected compared to the case of pristine PNRs. A comparison between the cyan and purple curves in Fig. 2(b) shows that in this case, the absolute value of the maxima is notably greater than that of the ZPNR counterpart. In Fig. 2(a), one can see that for the symmetric case, the first conductance plateau in ZPNR disappears completely, which is understood as an induced large band gap in the electronic conductance due to the suppression of the contribution of edge states. We have shown in Fig. 4(a) the electronic local density of states (LDOS) for a symmetric PRZL at $\mu = 0$ eV to clearly show the suppression of the edge modes contribution to the electronic conductance near connection regions. As a result, the peak value of the thermopower for this PRZL around zero chemical potential is enhanced to $58K_{\mathrm{B}}/e$ $(= 4988\,\mu\mathrm{V/K})$. On the other hand, for an asymmetric PRZL, the situation is different. Figure 4(b) displays the LDOS of electrons for this configuration at $\mu = 0$ eV. As seen, in this ringlike geometry a path between the electrodes is observed, and the original first conductance plateau still exists [see Fig. 2(a)], though its height decreases due to blocking the other path of edge modes propagation. While the enhancement of the maximum power factor in asymmetric PRZL [orange curve in Fig. 2(b)] compared to that of ZPNR may not be particularly significant, the key observation here is that nanorings exhibit significantly lower electronic thermal conductance κ_e [as shown in Fig. 2(d)] compared to ZPNR. Consequently, our designed phosphorene-based nanostructures have the potential to improve the figure of merit ZT.

Next, we examine the thermoelectric performance of a phosphorene ring with armchair leads (PRAL). Figure 3 depicts the same quantities as in Fig. 2 for both asymmetric (orange curves) and symmetric (purple curves) connection of leads. A comparison between the two nanostructures reveals a significant reduction in electronic conductance for the symmetric PRAL compared to the asymmetric case. To offer additional insight into our statement, we have shown in Fig. 5 the spatial LDOS of the transport modes at $\mu = 2$ eV. As seen in the symmetric case [Fig. 5(a)], the wave packets of electrons primarily reside within the attached left and right leads, with fewer bound states found in the central device. This reduces the propagation probability of electrons from the left lead to the right one or vice versa. On the other hand, the LDOS of the asymmetric configuration [Fig. 5(b)] exhibits more bounding states in the central device, and thus it increases the probability of electron transmission which emerges as conductance peaks. In the case of the asymmetric PRAL, the band gap remains nearly unchanged, resulting in a similar SC compared to APNR. Interestingly, for the symmetric PRAL, a remarkable enhancement in the band gap can be observed, leading to an increased maximum value of the SC. It is intriguing to note that the symmetric PRAL exhibits an electronic thermal conductance [purple curve in Fig. 3(d)] more than one order of magnitude smaller than that of APNRs at the corresponding location of the maximum power factor. Consequently, one can anticipate a significant enhancement in the TE performance for these phosphorene-based nanostructures.

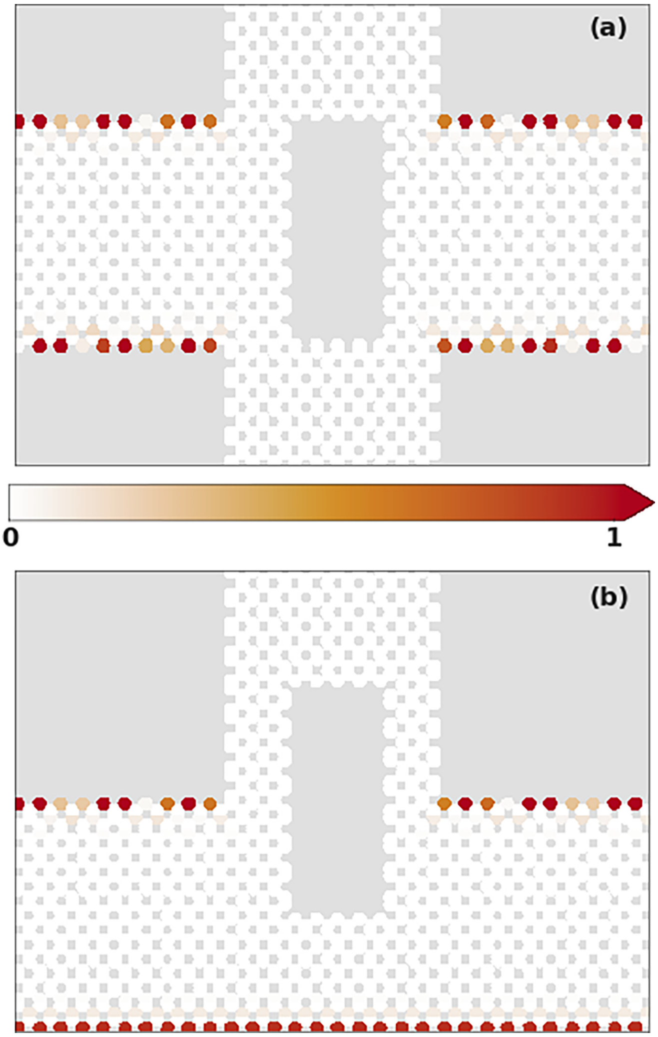

FIG. 4. Spatial LDOS for (a) a symmetric and (b) an asymmetric PRZL at $\mu = 0$ eV. The parameters used are the same as in Fig. 2. The color bar denotes the electronic density distribution across the device.

Now, let us investigate the influence of the nanoring size on the electronic conductance and thermopower of PRZLs. Our focus is on symmetric PRZLs. Figures 6(a)–6(d) illustrate the calculated electronic transport coefficients for two

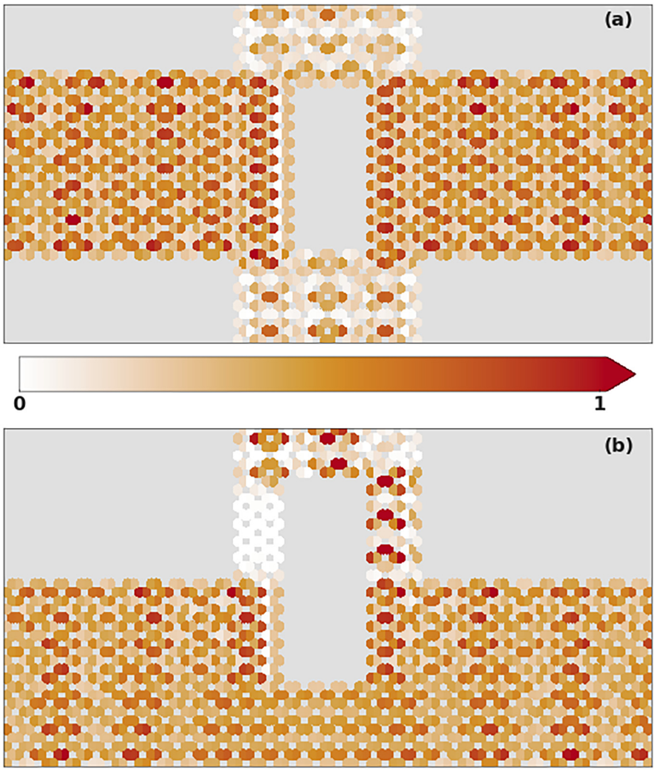

FIG. 5. Spatial LDOS for (a) a symmetric and (b) an asymmetric PRAL at $\mu = 2$ eV. The parameters used are the same as in Fig. 3. The color bar denotes the electronic density distribution across the device.

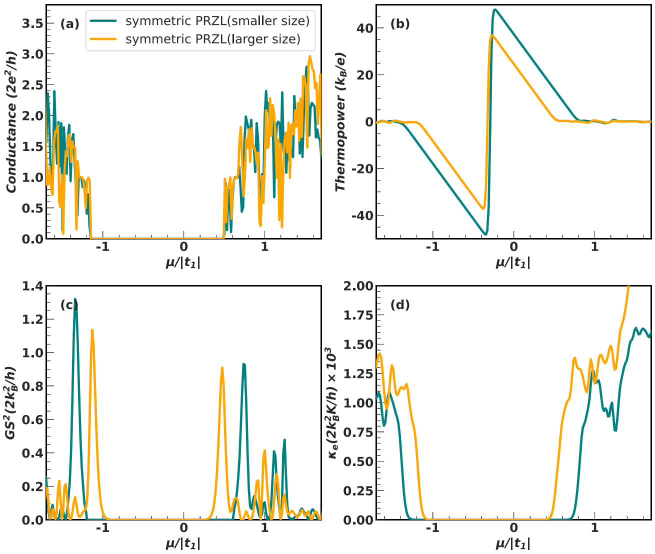

FIG. 6. Cyan curves show (a) electronic conductance, (b) thermopower, (c) power factor, and (d) electronic thermal conductance as a function of scaled chemical potential for a symmetric PRZL with a set of parameters $K_BT = 0.021|t_1|$, $W_{\text{in}} = 2.6$ nm, $L_{\text{in}} = 81$ nm, $W_{\text{out}} = 8.76$ nm, $L_{\text{out}} = 86.32$ nm, and $W_L = 4.38$ nm. Orange curves show the same quantities for another symmetric PRZL with the set of parameters $K_BT = 0.021|t_1|$, $W_{\text{in}} = L_{\text{in}} = W_{\text{out}}/2 = L_{\text{out}}/2 = W_L = 4.38$ nm.

symmetric PRZLs with different sizes. The orange and cyan curves show the results for the first set of parameters $W_{\text{in}} = 2.6$ nm, $L_{\text{in}} = 81$ nm, $W_{\text{out}} = 8.76$ nm, $L_{\text{out}} = 86.32$ nm, and $W_L = 4.38$ nm, and the second set of structure parameters $W_{\text{in}} = L_{\text{in}} = W_{\text{out}}/2 = L_{\text{out}}/2 = W_L = 4.38$ nm, respectively. The results clearly show that the thermopower depends significantly on the size of the considered nanorings. In general, the smaller the ring, the better TE response we get. For instance, in the second case, the maxima S enhances and leads to a peak value of 48 K_B/e (= 4128 μV/K) at zero energy.

In addition, the SC spectrum of the PRZL exhibits some other small oscillations at higher chemical potentials, yielding changes in the sign. Figures 7(a) and 7(b) show a zoomed-in view of Figs. 6(a) and 6(b) (cyan curves) in the scaled chemical potential of 1.37–1.48. As seen, the transmission coefficient exhibits Fano resonances and/or antiresonances that do not exist in ZPNRs. We show in Fig. 7(c) the LDOS of the Fano resonance peak. The reason behind the appearance of Fano resonance peaks is the interaction between the electronic states of the ring and connected leads. As seen, the mentioned LDOS shows localized states in some regions of the ring, implying that the Fano resonances are closely related to the appearance of these bound states [42]. Theoretically, the complexity of a system can be reduced while preserving the underlying physics of Fano resonances and/or antiresonances by using the transformative capabilities of the decimation method [43–46]. By following the formal procedure of this method, our configurations can be perceived as an effective quantum wire and an array of side-coupled effective quantum dots. Due to the hybridization and renormalization effects that occur during the decimation process, the hopping integrals and on-site energies of the nanostructure can undergo changes. These modifications give rise to the emergence of new effective quantities in the simplified system. The schemes shown in Figs. 8(a) and 8(c) represent two simplified models that are similar in nature to our symmetric and antisymmetric configurations.

We first examine a symmetrical configuration in which two effective impurity sites labeled as 1 and 2 form a double quantum dot. These sites are connected to left and right leads, as shown in Fig. 8(a). In this model, each site is assumed to possess a single energy level, and we neglect interdot and intradot electron-electron interactions. The total Hamiltonian of the system can be expressed as $\mathcal{H} = \mathcal{H}_{\text{D}} + \mathcal{H}_{\text{leads}} + \mathcal{H}_{\text{tunneling}}$. Here, $\mathcal{H}_{\text{D}}$ is the Hamiltonian of the two-impurity sites, with the assumption that there is no tunneling coupling between them:

$$\mathcal{H}_{\text{D}} = \sum_{i=1}^{2} \varepsilon_i d_i^\dagger d_i. \tag{14}$$

Also, $\mathcal{H}_{\text{leads}}$ describes the dynamic of leads, and $\mathcal{H}_{\text{tunneling}}$ accounts for the tunneling between impurity sites and leads by the tunneling couplings $\Gamma_{\text{L(R)}}$. By assuming that the Green's functions of the leads are imaginary around the energy ε_0 and show minimal dependence on energy in this region, we can make use of the wide-band approximation [47]. Consequently, the self-energy can be expressed as $\Sigma_{\text{L(R)}}^{r(a)}(E) = \mp i\Gamma_{\text{L(R)}}/2$. Therefore, using Eqs. (8) and (14), the inverse of the retarded

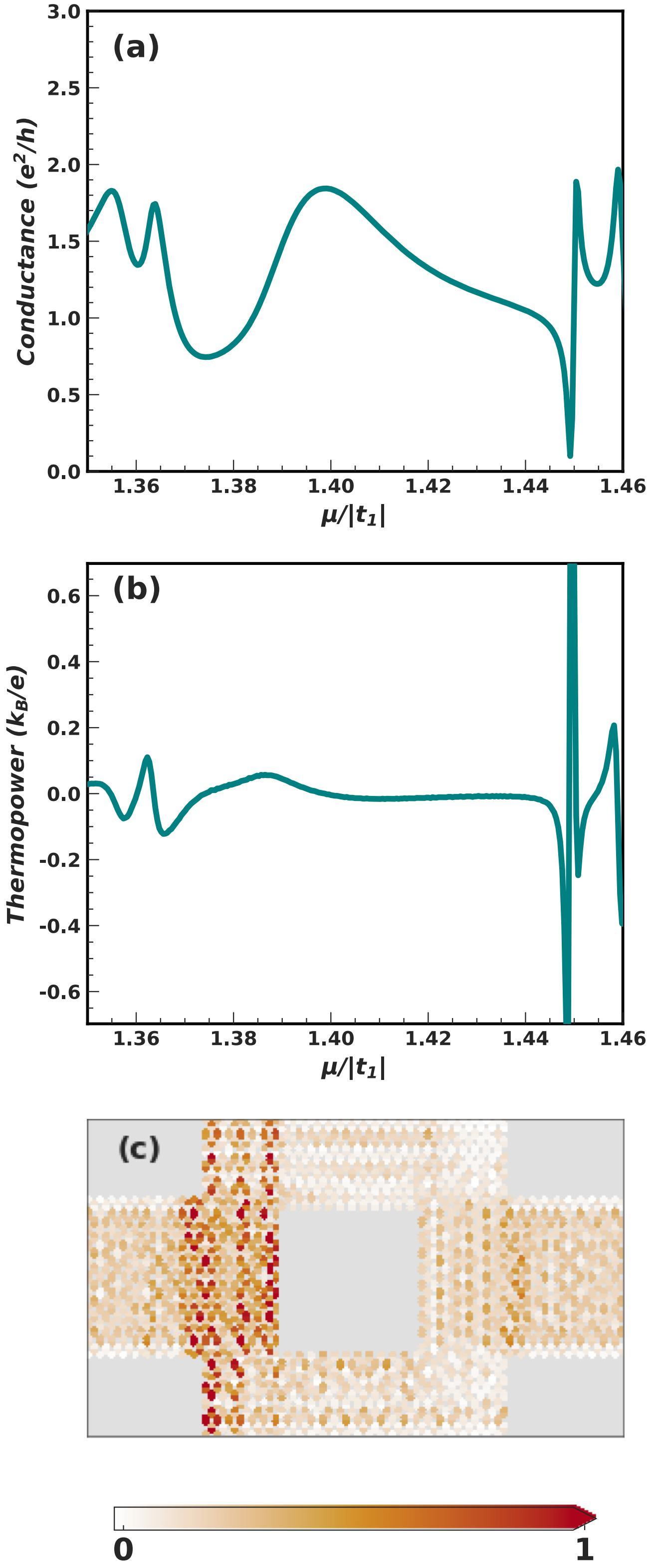

FIG. 7. (a) and (b) Zoomed-in views of Figs. 6(a) and 6(b) in the scaled chemical potential of 1.37–1.48. (c) LDOS at the Fano resonance peak.

Green's function for the central region is written as

$$[G_{\rm D}^r]^{-1} = \begin{pmatrix} E^r - \varepsilon_1 + \frac{i}{2}\Gamma_{11} & \frac{i}{2}\Gamma_{12} \\ \frac{i}{2}\Gamma_{21} & E^r - \varepsilon_2 + \frac{i}{2}\Gamma_{22} \end{pmatrix}, \tag{15}$$

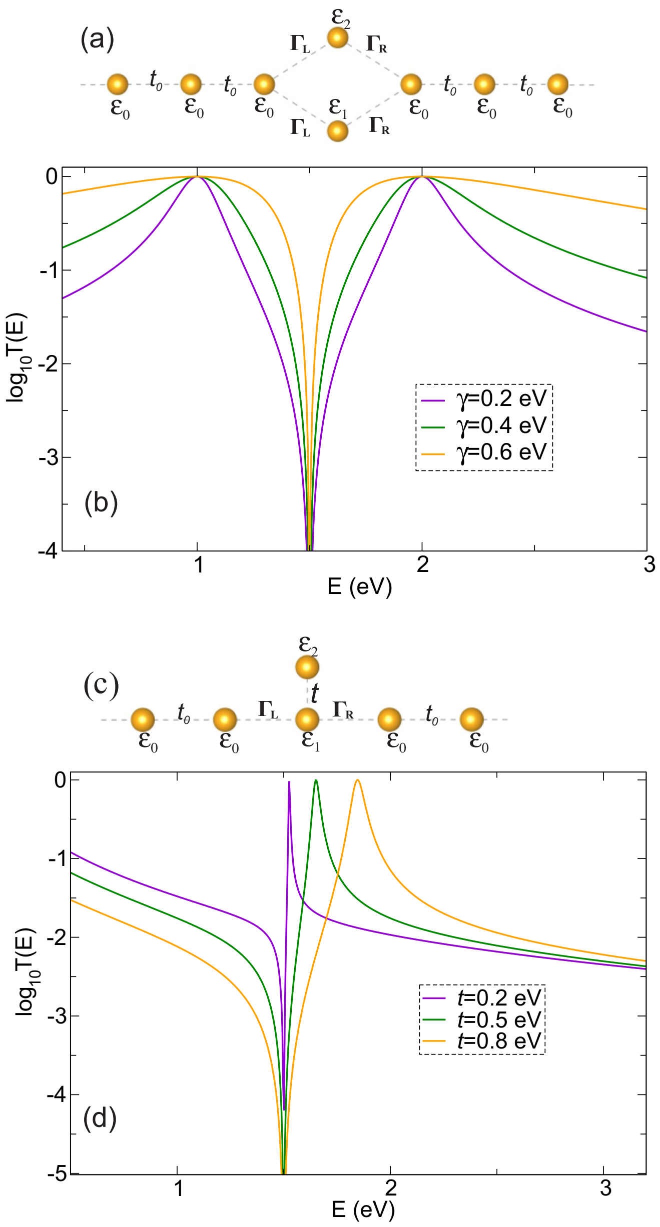

FIG. 8. Two semi-finite 1D chains are connected in (a) symmetric and (c) asymmetric configurations to scattering regions. The scattering regions have two single-level site energies ε_1 and ε_2, and they are connected to the chains through couplings $\Gamma_{\rm L}$ and $\Gamma_{\rm R}$. (b) Semilog plot of the transmission probability as a function of energy for configuration (a) for $\varepsilon_1 = 1$ eV, $\varepsilon_2 = 2$ eV, and different values of γ. (d) The same quantity for $\Gamma_{\rm L} = \Gamma_{\rm R} = 0.2$ eV, $\varepsilon_0 = 0$ eV, $\varepsilon = 1.5$ eV, and various values of the coupling t.

where $\Gamma_{ij} = \Gamma_{ij{\rm L}} + \Gamma_{ij{\rm R}}$. In this symmetrical configuration, both the diagonal and nondiagonal matrix elements of the matrices $\Gamma_{\rm L(R)}$ have equal values, denoted as $\Gamma_{ij{\rm L(R)}} = \gamma_{\rm L\,(R)}$. From Eq. (15), the retarded Green's function is given by

$$G_{\rm D}^r = \frac{1}{\Lambda}\begin{pmatrix} E^r - \varepsilon_2 + \frac{i}{2}\gamma & \frac{i}{2}\gamma \\ \frac{i}{2}\gamma & E^r - \varepsilon_1 + \frac{i}{2}\gamma \end{pmatrix}, \tag{16}$$

where $\Lambda = (E^r - \varepsilon_1)(E^r - \varepsilon_2) + i\gamma(E^r - \overline{\varepsilon})$, $\gamma = \gamma_{\rm L} + \gamma_{\rm R}$, and $\overline{\varepsilon} = (\varepsilon_1 + \varepsilon_2)/2$. Subsequently, the advanced Green's function can be obtained directly using Eq. (16). Upon inserting them into Eq. (9) and performing a straightforward calculation, the electron transmission is determined as

$$T(E)=\frac{4\gamma_{\mathrm{L}}\gamma_{\mathrm{R}}}{[(E-\varepsilon_1)(E-\varepsilon_2)/(E-\overline{\varepsilon})]^2+\gamma^2}. \tag{17}$$

Figure 8(b) illustrates the semilog plot of the transmission probability as a function of energy for $\varepsilon_1 = 1$ eV, $\varepsilon_2 = 2$ eV, and different values of γ. As seen, the prominent characteristic observed in this model is the occurrence of an antiresonance at $E = \overline{\varepsilon}$, where the transmission completely vanishes. This phenomenon occurs due to a destructive quantum interference between the paths involving impurity levels 1 and 2. Hence, the interference mechanism in our system can be clarified by employing this simple model, enabling us to gain a basic understanding of the fundamental factors that contribute to the characteristics of conductance, including the emergence of antiresonance phenomena.

Now, let us consider an asymmetric single-channel configuration, which consists of two semi-infinite 1D leads connected to impurity sites 1 and 2 [see Fig. 8(c)]. Similarly, the system can be characterized by the total Hamiltonian $\mathcal{H} = \mathcal{H}_{\mathrm{D}} + \mathcal{H}_{\mathrm{leads}} + \mathcal{H}_{\mathrm{tunneling}}$. In this configuration, the Hamiltonian of two-impurity sites is written as

$$\mathcal{H}_{\mathrm{D}}=\sum_{i=1}^{2}\varepsilon_i d_i^\dagger d_i + t(d_2^\dagger d_1 + d_1^\dagger d_2), \tag{18}$$

where the coupling between them is described by the tunneling coupling t. The dynamics of the leads is described by $\mathcal{H}_{\mathrm{leads}}$, while $\Gamma_{\mathrm{L(R)}}$ takes into account the tunneling between impurity site 1 and the leads through the tunneling couplings $\mathcal{H}_{\mathrm{tunneling}}$. Thus, by utilizing Eqs. (8) and (14), we can express the inverse of the retarded Green's function of the central region as

$$\left[G_{\mathrm{D}}^r\right]^{-1}=\begin{pmatrix} E^r-\varepsilon_0 & -t \\ -t & E^r-\varepsilon \end{pmatrix}+\frac{i}{2}\begin{pmatrix} \Gamma_{11} & 0 \\ 0 & 0 \end{pmatrix}, \tag{19}$$

where $\Gamma = \Gamma_{\mathrm{L}} + \Gamma_{\mathrm{R}}$. By employing Eq. (9), we can easily demonstrate that the zero-bias transmission is expressed as $T(E) = \Gamma_{\mathrm{L}}\Gamma_{\mathrm{R}}|G_{11}^r|^2$, where $G_{11}^r = (E^r-\varepsilon)/\{(E^r-\varepsilon_0+i\frac{\Gamma_{\mathrm{L(R)}}}{2})-(E^r-\varepsilon)\}$ represents the retarded Green's function at the impurity site 1. This result directly leads to the transmission function

$$T(E)=\frac{4\Gamma_{\mathrm{L}}\Gamma_{\mathrm{R}}}{4[E-\varepsilon_0-t^2/(E-\varepsilon)]^2+\Gamma^2}. \tag{20}$$

We have shown in Fig. 8(d) the semilog plot of the transmission probability as a function of energy for $\Gamma_{\mathrm{L}} = \Gamma_{\mathrm{R}} = 0.2$ eV, $\varepsilon_0 = 0$ eV, $\varepsilon = 1.5$ eV, and various values of the coupling t. In this model, a notable feature is the presence of an antiresonance at $E = \varepsilon$, resulting in a complete suppression of transmission. This behavior can be attributed to a destructive quantum interference between the direct path passing through impurity level 1 and an alternative path involving the coupled site. Additionally, in proximity to the antiresonance, a Fano peak emerges, which can enhance the thermoelectric properties of the system. This can be understood as follows. Take the chemical potential near a Fano-like antiresonance. According to Eq. (12), the thermopower S is proportional to K_1, whose value is assessed by the integrand $(-\frac{\partial f_0}{\partial E})(E-\mu)T_{LR}(E)$, where $(E-\mu)$ is an odd function around μ. As a result, a larger asymmetry of transmission coefficient $T_{LR}(E)$ leads to an increase in K_1, and thus a higher TE response. Such behavior is evident in Fig. 7(b), which shows the behavior of the SC near the Fano-like antiresonance. Such behavior of the SC near the Fano-like antiresonance is also evident for our symmetric PRZL, as shown in Fig. 7(b).

Given the availability of electronic transport quantities, it is important to assess the impact of thermal conductance on the figure of merit in our lead-nanoring-lead systems. This aspect holds significance as there is a reduction in thermal conductivity caused by phonon scattering at the boundaries. The ballistic thermal conductance of a nanoribbon of width W is given by [48]

$$G_{\mathrm{ph}}=\frac{k_{\mathrm{B}}^2 T}{h}\int_0^\infty\left(\frac{M\lambda}{L+\lambda}\right)_{\mathrm{ph}}\frac{x^2e^x}{(e^x-1)^2}dx, \tag{21}$$

where M represents the number of phonon modes, λ corresponds to the mean free path of phonons, and $x \equiv \hbar\omega/k_{\mathrm{B}}T$. Using this equation, we can express the thermal conductance in the ballistic limit ($L \ll \lambda$) as follows:

$$G_{\mathrm{ph}}^b=\frac{k_{\mathrm{B}}^2 T}{h}\int_0^\infty M_{\mathrm{ph}}\frac{x^2e^x}{(e^x-1)^2}dx. \tag{22}$$

To examine how the thermal conductance depends on temperature and sample width, we evaluate the number of phonon modes that contribute to the thermal transport. It has been shown that the number of phonon modes is directly related to the number of wavelengths that can fit within the cross section of the nanoribbon [48]:

$$M_{\mathrm{ph}}\simeq\frac{2W}{h/p}\times N_{\mathrm{aco}}=2N_{\mathrm{aco}}\frac{W}{\lambda_{\mathrm{aco}}}. \tag{23}$$

Note that in monolayer phosphorene, it is known that acoustic phonons play a major role in phonon transport at room temperature [49]. Therefore, we focus solely on their contribution in our analysis. By using the relation $\lambda_{\mathrm{aco}} = 2\pi v_{\mathrm{aco}}/\omega$, where v_{aco} represents the acoustic phonon velocity, we can rewrite Eq. (23) as follows:

$$M_{\mathrm{ph}}\simeq\frac{2N_{\mathrm{aco}}k_{\mathrm{B}}TW}{hv_{\mathrm{aco}}}x. \tag{24}$$

By substituting this relation into Eq. (22) and evaluating the corresponding integral, we obtain

$$G_{\mathrm{ph}}^b\simeq 12\zeta(3)N_{\mathrm{aco}}\frac{k_{\mathrm{B}}^3T^2W}{h^2v_{\mathrm{aco}}}, \tag{25}$$

where $\zeta(3)$ is the Riemann zeta function at 3 and its numerical value is $\simeq 1.20$. Although this approximation may not accurately capture the temperature dependence over a wide temperature range, it predicts a linear relationship between the thermal conductance and the width of phosphorene nanoribbons, which is in very good agreement with other works [50,51]. First-principles studies [49] have demonstrated that the longitudinal acoustic branch along the zigzag direction, characterized by a group velocity of ~7.8 km/s [49,52], plays a dominant role in determining the phonon thermal conductivity of phosphorene. Hence, by substituting numerical values into Eq. (25) at $T = 300$ K, we obtain

$$G_{\text{ph}}^{b} \simeq 0.98W\ (\text{nW / K}), \tag{26}$$

where W is written in units of nm. This result is in good agreement with the findings obtained using the nonequilibrium Green's-function method, where the thermal phonon transport along the zigzag direction is characterized by $G_{\text{ph}}^{b} \simeq 1.31W + 0.07\ (\text{nW / K})$ [50].

During the process of heat transfer in our rectangular rings, phonons, which play a crucial role in thermal transport, encounter interfaces and boundaries. These irregularities make the phonons scatter and deflect from their original paths, hindering their overall propagation. Therefore, this scattering mechanism disrupts the coherent flow of heat, leading to a reduction in the thermal conductivity of the system. In this situation, we can envision a rectangular nanoring in a mesoscopic-like regime, where the mean free path of phonons becomes comparable to the nanoring size due to scattering at the boundaries. In this regime, the phonon thermal conductance can be defined for a nanoring with an effectively one-dimensional cross-section of width W_{eff} as [48]

$$G_{\text{ph}}^{r} = \kappa_{\text{ph}}^{r} \frac{W_{\text{eff}}}{L_{\text{eff}} + \lambda_{\text{eff}}}, \tag{27}$$

where κ_{ph}^{r}, L_{eff}, and λ_{eff} represent the phonon thermal conductivity, the effective size, and the effective phonon mean free path of the rectangular ring, respectively. We can estimate the decrease in thermal conductivity in our rectangular nanoring by adjusting the thermal conductivity of a nanoribbon at its ballistic limit using a single parametric function [49,53]

$$\kappa_{\text{ph}}^{r} \simeq \frac{\kappa_{\text{ph}}^{b}}{1 + l_0/L_{\text{eff}}}, \tag{28}$$

where l_0 is a parameter. For phosphorene, we adopt the values of 66 and 83 nm for the parameter l_0 in the zigzag and armchair directions, respectively [49]. Using Eq. (28), we rewrite Eq. (27) in the form

$$G_{\text{ph}}^{r} \simeq \frac{1}{(1 + l_0/L_{\text{eff}})(1 + L_{\text{eff}}/\lambda_{\text{eff}})} G_{\text{ph}}^{b}, \tag{29}$$

where Eq. (26) can be used for ZPNRs. For symmetric and asymmetric attachment configurations, we define the effective mean free path within rings as $L_{\text{eff}}^{\text{sym}} = (L_{\text{out}} + W_{\text{out}} - W_{\text{in}})/3$ and $L_{\text{eff}}^{\text{asym}} = (2L_{\text{out}} + W_{\text{out}} - W_{\text{in}})/4$, respectively.

By utilizing the aforementioned estimations and the numerically calculated electronic transport quantities for our systems, we can estimate the figure of merit ZT using the equation

$$ZT = \frac{GS^2}{\kappa_e + G_{\text{ph}}^{r}} T. \tag{30}$$

(Note that when using this equation, we perform a unit transformation [nW/K → $1741(2k_B^2\text{K}/h)$] for G_{ph}^{r}.)

Figure 9(a) illustrates the calculated figure of merit at room temperature for described systems in Fig. 2. In our calculations, we used Eq. (26) to evaluate the thermal conductance of the ZPNR. As observed, the enhancement in thermoelectric properties resulting from electron contribution, along with the decrease in thermal conductance in both configurations, has led to a significant increase in the maximum figure of merit.

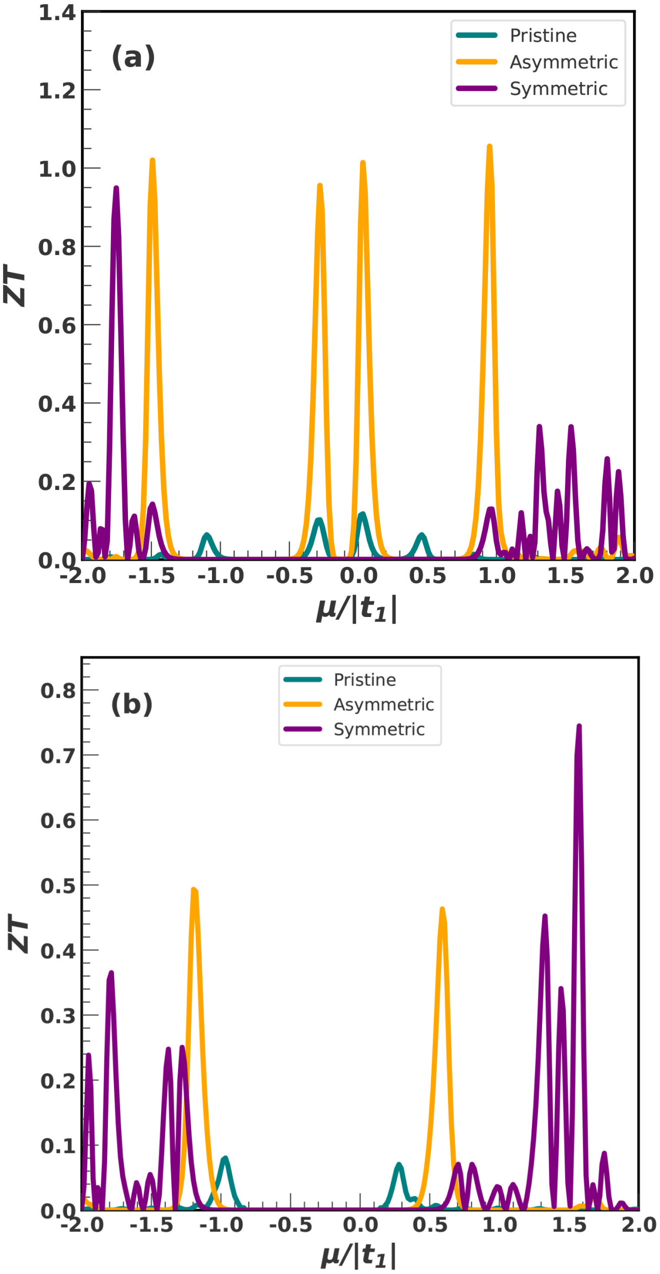

FIG. 9. (a) and (b) Dimensionless figure of merit ZT as a function of scaled chemical potential for systems as described in Figs. 2 and 3, respectively.

For APNRs, we employ the relation $G_{\text{ph}}^{b} \simeq 0.39W + 0.05$ (nW/K) extracted from the data presented in Ref. [50]. We present in Fig. 9(b) the corresponding figure of merit for systems with parameters described in Fig. 3. Our result reveals a remarkable enhancement in the maximum figure of merit for both symmetric and asymmetric PRALs compared to corresponding APNR.

Finally, we examine the effect of applying a perpendicular magnetic field on the TE performance of a PRZL. By applying a perpendicular magnetic field B to the plane of a MLP nanoring, the hopping parameters t_{ij} in Eq. (1) are modified as

$$t_{ij} \rightarrow t_{ij} \exp\left(i \frac{2\pi e}{h} \int_{\mathbf{r_i}}^{\mathbf{r_j}} \mathbf{A} \cdot \mathbf{dl}\right), \tag{31}$$

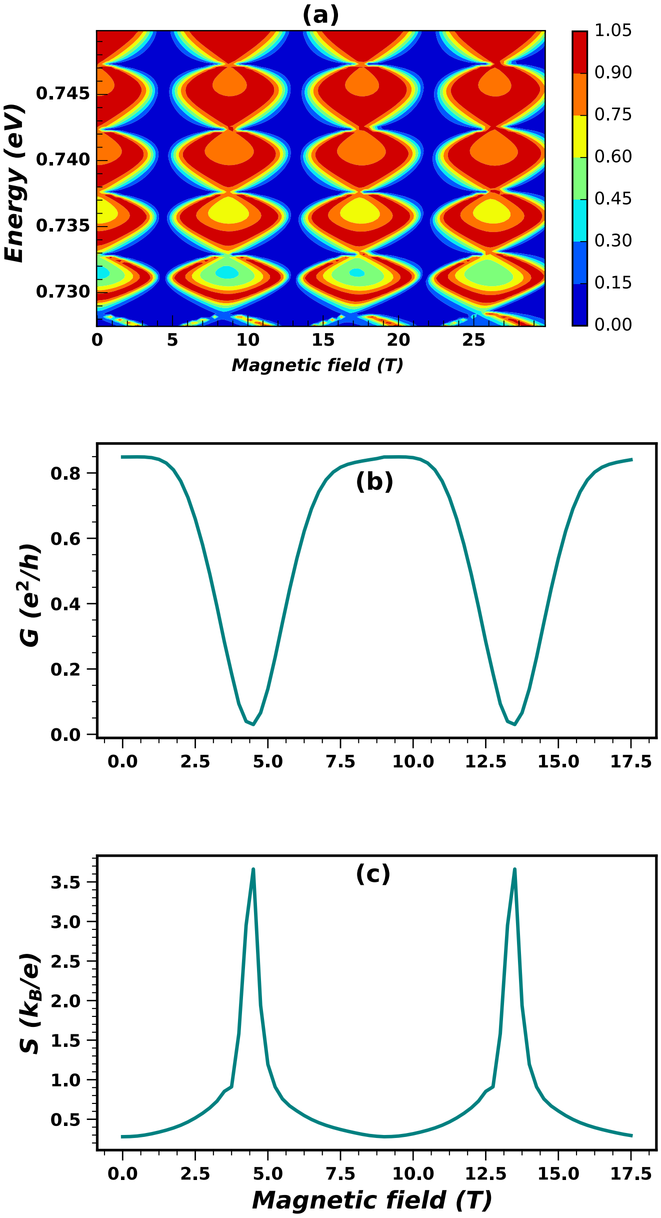

FIG. 10. (a) Contour plot of the electronic conductance as a function of the applied magnetic field and the Fermi energy for a symmetric PRZL. The set of parameters are $K_{\rm B}T = 0.021|t_1|$, $W_{\rm in} = 2.6$ nm, $L_{\rm in} = 81$ nm, $W_{\rm out} = 8.76$ nm, $L_{\rm out} = 86.32$ nm, and $W_L = 4.38$ nm. The electronic conductance (b) and thermopower (c) of the symmetric PRZL at $E_f = 0.732$ eV.

in order to include Peierl's phase factor, where **A** is the vector potential. It has been shown [5] that by applying a perpendicular magnetic field to PNRs, the conductance experiences dramatic oscillations at special Fermi energies, leading to a giant magnetoresistance (MR) in zigzag PNRs. Here, we show that the TE performance of a PRZL is highly dependent on the magnetic flux. We only focus on the symmetric case because in this configuration the thermopower changes more rapidly compared to the ZPNRs. Figure 10(a) depicts the contour plot of the conductance as a function of the applied magnetic field and the Fermi energy for a symmetric PRZL with structure parameters $K_{\rm B}T = 0.021|t_1|$, $W_{\rm in} = 2.6$ nm, $L_{\rm in} = 81$ nm, $W_{\rm out} = 8.76$ nm, $L_{\rm out} = 86.32$ nm, and $W_L = 4.38$ nm. Note that here we have increased the size of the nanoring to reduce its oscillation period in the presence of the magnetic field. In this situation, the effective area of the nanoring is relatively large, and as a result, the period of AB oscillations is small, which makes it experimentally feasible. We approximate the period of oscillation as $\Delta B = 2\pi\phi_0/\bar{S}$, where $\bar{S} = (S_{\rm in} + S_{\rm out})/2$ is the average area of the outer and inner nanorings [54]. In our case, the average area is 472.41 nm^2, resulting in an oscillation period of $\Delta B \approx 8.73$ T. As seen in Fig. 10(a), the conductance exhibits an oscillative behavior as a function of the applied magnetic field with a period of ~8.7 T, which agrees very well with our theoretical prediction. As seen from Figs. 10(b) and 10(c), the electronic conductance G and the thermopower S also have a periodic character by changing the magnetic field. This leads to a drastic increase in the thermopower S near an antiresonance point. Two salient features that we realize from these figures are the high tunability of the thermopower and the possibility to switch on and off the thermoelectric response of the phosphorene nanoring with the magnetic flux. Remarkably, the differential SC can be about eight times larger than the one in the absence of the magnetic field. This confirms the excellent thermoelectric response of this phase-coherent mesoscopic device, making it a promising quantum heat engine in a closed-circuit configuration [55].

IV. SUMMARY AND CONCLUSION

In summary, we investigated the thermoelectric properties of different phosphorene nanorings with symmetrical or asymmetrical connected leads. We utilized the effective low-energy TB model of monolayer phosphorene to construct the TB Hamiltonian of our devices and to characterize their electronic conductance, thermopower, and thermal conductance within the Landauer-Büttiker formalism. Our results showed that quantum interference of localized electronic states in the nanorings and the electronic wave packets in the leads profoundly affect the TE properties of the system. We found that for a symmetrical connection of zigzag leads to rectangular rings, the original first conductance plateau completely collapses due to the suppression of the contribution of edge states. This induces a wide gap in the system, giving rise to dramatically enhanced peak values in thermopower of such configurations. We also showed that the TE performance of these systems depends on the size of the ring, and one can reach maximum thermopowers of ~5000 μV/K. Interestingly, we realized that the substantial decrease in electronic and phononic thermal conductance for both symmetric and asymmetric connection of zigzag leads results in a remarkable enhancement in the figure of merit. Furthermore, in the case of asymmetric connection setups with armchair-edged leads, we observed that although the thermopower remains almost intact, there was a significant reduction in both electronic and phononic thermal conductance, resulting in a noteworthy improvement in the figure of merit. Moreover, the Fano antiresonances that appeared in the quantum conductance of phosphorene nanorings lead to characteristic features in the Seebeck coefficient. We showed the tunability of the thermopower and the possibility to switch on and off the thermoelectric response of phosphorene nanorings by an applied magnetic field. Our study confirmed the promising thermoelectric properties of these phase-coherent mesoscopic devices, and we propose them as potential thermoelectric candidates.

ACKNOWLEDGMENTS

Part of the research was funded within the framework of the HSE University Basic Research Program.

F.M.B. and E.T.S. contributed equally to this work.

---

[1] I. Petsagkourakis, K. Tybrandt, X. Crispin, I. Ohkubo, N. Satoh, and T. Mori, Thermoelectric materials and applications for energy harvesting power generation, Sci. Tech. Adv. Mater. **19**, 836 (2018).

[2] J. R. Szczech, J. M. Higgins, and S. Jin, Enhancement of the thermoelectric properties in nanoscale and nanostructured materials, J. Mater. Chem. **21**, 4037 (2011).

[3] C. Hozana and A. Latgé, Thermoelectric properties of nanostructured systems based on narrow arm-chair graphene nanoribbons, J. Phys.: Condens. Matter **31**, 125303 (2019).

[4] F. Mazzamuto, V. Hung Nguyen, Y. Apertet, C. Caër, C. Chassat, J. Saint-Martin, and P. Dollfus, Enhanced thermoelectric properties in graphene nanoribbons by resonant tunneling of electrons, Phys. Rev. B **83**, 235426 (2011).

[5] R. Zhang, Z. Wu, X. J. Li, and K. Chang, Aharonov-Bohm effect in monolayer phosphorene nanorings, Phys. Rev. B **95**, 125418 (2017).

[6] Y. Liu and X. Yang, Enhancement of thermoelectric efficiency in a double-quantum-dot molecular junction, J. Appl. Phys. **108**, 023710 (2010).

[7] G. Haack and F. Giazotto, Efficient and tunable Aharonov-Bohm quantum heat engine, Phys. Rev. B **100**, 235442 (2019).

[8] E. Samuel Reich, Phosphorene excites materials scientists, Nature **506**, 19 (2014).

[9] L. Li, F. Yang, G. J. Ye, Z. Zhang, Z. Zhu, W. Lou, X. Zhou, L. Li, K. Watanabe, T. Taniguchi *et al.*, Quantum Hall effect in black phosphorus two-dimensional electron system, Nat. Nanotech. **11**, 593 (2016).

[10] L. Li, Y. Yu, G. J. Ye, Q. Ge, X. Ou, H. Wu, D. Feng, X. H. Chen, and Y. Zhang, Black phosphorus field-effect transistors, Nat. Nanotech. **9**, 372 (2014).

[11] H. Liu, A. T. Neal, Z. Zhu, Z. Luo, X. Xu, D. Tománek, and P. D. Ye, Phosphorene: An unexplored 2d semiconductor with a high hole mobility, ACS Nano **8**, 4033 (2014).

[12] F. Xia, H. Wang, and Y. Jia, Rediscovering black phosphorus as an anisotropic layered material for optoelectronics and electronics, Nat. Commun. **5**, 4458 (2014).

[13] A. Castellanos-Gomez, L. Vicarelli, E. Prada, J. O. Island, K. Narasimha-Acharya, S. I. Blanter, D. J. Groenendijk, M. Buscema, G. A. Steele, J. Alvarez *et al.*, Isolation and characterization of few-layer black phosphorus, 2D Mater. **1**, 025001 (2014).

[14] S. P. Koenig, R. A. Doganov, H. Schmidt, A. Castro Neto, and B. Özyilmaz, Electric field effect in ultrathin black phosphorus, Appl. Phys. Lett. **104**, 103106 (2014).

[15] J. Qiao, X. Kong, Z.-X. Hu, F. Yang, and W. Ji, High-mobility transport anisotropy and linear dichroism in few-layer black phosphorus, Nat. Commun. **5**, 4475 (2014).

[16] M. Buscema, D. J. Groenendijk, S. I. Blanter, G. A. Steele, H. S. Van Der Zant, and A. Castellanos-Gomez, Fast and broadband photoresponse of few-layer black phosphorus field-effect transistors, Nano Lett. **14**, 3347 (2014).

[17] S. Das, W. Zhang, M. Demarteau, A. Hoffmann, M. Dubey, and A. Roelofs, Tunable transport gap in phosphorene, Nano Lett. **14**, 5733 (2014).

[18] W. Lu, H. Nan, J. Hong, Y. Chen, C. Zhu, Z. Liang, X. Ma, Z. Ni, C. Jin, and Z. Zhang, Plasma-assisted fabrication of monolayer phosphorene and its raman characterization, Nano Res. **7**, 853 (2014).

[19] A. S. Rodin, A. Carvalho, and A. H. Castro Neto, Strain-Induced Gap Modification in Black Phosphorus, Phys. Rev. Lett. **112**, 176801 (2014).

[20] X. Chen, Y. Wu, Z. Wu, Y. Han, S. Xu, L. Wang, W. Ye, T. Han, Y. He, Y.-a. Cai *et al.*, High-quality sandwiched black phosphorus heterostructure and its quantum oscillations, Nat. Commun. **6**, 7315 (2015).

[21] V. Tayari, N. Hemsworth, I. Fakih, A. Favron, E. Gaufrès, G. Gervais, R. Martel, and T. Szkopek, Two-dimensional magnetotransport in a black phosphorus naked quantum well, Nat. Commun. **6**, 7702 (2015).

[22] Y.-L. Zou, J. Song, C. Bai, and K. Chang, Impurity scattering and friedel oscillations in monolayer black phosphorus, Phys. Rev. B **94**, 035431 (2016).

[23] Q. Wei and X. Peng, Superior mechanical flexibility of phosphorene and few-layer black phos-phorus, Appl. Phys. Lett. **104**, 251915 (2014).

[24] J. O. Island, G. A. Steele, H. S. van der Zant, and A. Castellanos-Gomez, Environmental instability of few-layer black phosphorus, 2D Mater. **2**, 011002 (2015).

[25] M. Ezawa, Topological origin of quasi-flat edge band in phosphorene, New J. Phys. **16**, 115004 (2014).

[26] A. Castellanos-Gomez, Black phosphorus: Narrow gap, wide applications, J. Phys. Chem. Lett. **6**, 4280 (2015).

[27] E. Flores, J. R. Ares, A. Castellanos-Gomez, M. Barawi, I. J. Ferrer, and C. Sánchez, Thermoelectric power of bulk black-phosphorus, Appl. Phys. Lett. **106**, 022102 (2015).

[28] Y. Saito, T. Iizuka, T. Koretsune, R. Arita, S. Shimizu, and Y. Iwasa, Gate-tuned thermoelectric power in black phosphorus, Nano Lett. **16**, 4819 (2016).

[29] A. Carvalho, M. Wang, X. Zhu, A. S. Rodin, H. Su, and A. H. Castro Neto, Phosphorene: From theory to applications, Nat. Rev. Mater. **1**, 16061 (2016).

[30] R. Fei, A. Faghaninia, R. Soklaski, J.-A. Yan, C. Lo, and L. Yang, Enhanced thermoelectric efficiency via orthogonal electrical and thermal conductances in phosphorene, Nano Lett. **14**, 6393 (2014).

[31] J. Zhang, H. Liu, L. Cheng, J. Wei, J. Liang, D. Fan, J. Shi, X. Tang, and Q. Zhang, Phosphorene nanoribbon as a promising candidate for thermoelectric applications, Sci. Rep. **4**, 6452 (2014).

[32] R. Ma, H. Geng, W. Y. Deng, M. N. Chen, L. Sheng, and D. Y. Xing, Effect of the edge states on the conductance and thermopower in zigzag phosphorene nanoribbons, Phys. Rev. B **94**, 125410 (2016).

[33] S. Lee, J.-P. Song, S.-H. Kang, and Y.-K. Kwon, Oxidation-enhanced thermoelectric efficiency in a two-dimensional phosphorene oxide, Sci. Rep. **11**, 18525 (2021).

[34] M. C. Watts, L. Picco, F. S. Russell-Pavier, P. L. Cullen, T. S. Miller, S. P. Bartuś, O. D. Payton, N. T. Skipper, V. Tileli, and C. A. Howard, Production of phosphorene nanoribbons, Nature **568**, 216 (2019).

[35] M. Saiz-Bretín, A. V. Malyshev, P. A. Orellana, and F. Domínguez-Adame, Enhancing thermoelectric properties of graphene quantum rings, Phys. Rev. B **91**, 085431 (2015).

[36] A. N. Rudenko and M. I. Katsnelson, Quasiparticle band structure and tight-binding model for single- and bilayer black phosphorus, Phys. Rev. B **89**, 201408(R) (2014).

[37] S. Datta, *Electronic Transport in Mesoscopic Systems* (Cambridge University Press, Cambridge, 1997).

[38] T. Ouisse, *Electron Transport in Nanostructures and Mesoscopic Devices: An Introduction* (Wiley, London, 2013).

[39] S.-H. Lv and Y.-X. Li, Effects of the edge states on conductance and thermopower for the bilayer graphene nanoribbons, J. Appl. Phys. **112**, 053701 (2012).

[40] D. Moldovan and F. Peeters, Pybinding: A Python package for tight-binding calculations, 2016 [Online]. Available: http://dx.doi.org/10.5281/zenodo.56818.

[41] C. W. Groth, M. Wimmer, A. R. Akhmerov, and X. Waintal, Kwant: A software package for quantum transport, New J. Phys. **16**, 063065 (2014).

[42] R. Zhang, Z. Wu, X. Li, L. Li, Q. Chen, Y.-M. Li, and F. Peeters, Fano resonances in bilayer phosphorene nanoring, Nanotechnology **29**, 215202 (2018).

[43] T. S. Rodemund, F. Teichert, M. Hentschel, and J. Schuster, Quantum transport in graphene nanoribbon networks: Complexity reduction by a network decimation algorithm, New J. Phys. **25**, 013001 (2023).

[44] J. Ojeda, C. Duque, and D. Laroze, Transport properties through an aromatic molecular wire, Org. Electron. **41**, 369 (2017).

[45] J. H. Ojeda Silva, J. S. Paez Barbosa, and C. A. Duque Echeverri, Thermo-electrical conduction of the 2, 7-di ([1, 1′-biphenyl]-4-yl)-9h-fluorene molecular system: Coupling between benzene rings and stereoelectronic effects, Molecules **25**, 3215 (2020).

[46] J. H. Ojeda Silva, J. C. Cortés Peñaranda, J. A. Gómez Castaño, and C. A. Duque, Current's fluctuations through molecular wires composed of thiophene rings, Molecules **23**, 881 (2018).

[47] J. C. Cuevas and E. Scheer, *Molecular Electronics: An Introduction to Theory and Experiment* (World Scientific, Singapore, 2010).

[48] S. Datta, *Lessons from Nanoelectronics: A New Perspective on Transport-Part B: Quantum Transport* (World Scientific, Singapore, 2018).

[49] G. Qin, Q.-B. Yan, Z. Qin, S.-Y. Yue, M. Hu, and G. Su, Anisotropic intrinsic lattice thermal conductivity of phosphorene from first principles, Phys. Chem. Chem. Phys. **17**, 4854 (2015).

[50] W. Cao, H. Xiao, T. Ouyang, Z. Wang, and R. Xiong, Ballistic thermal transport in black and blue phosphorene nanoribbons and in-plane heterostructures, Phys. Lett. A **383**, 1493 (2019).

[51] M. Mahnama, M. Meshkinghalam, and M. Ozmaian, Anisotropic thermal conductivity and corrugated patterns in single-layer black phosphorus nanoribbon subjected to shear loading: A molecular dynamics study, J. Phys.: Condens. Matter **34**, 075403 (2022).

[52] Z. Zhu and D. Tománek, Semiconducting Layered Blue Phosphorus: A Computational Study, Phys. Rev. Lett. **112**, 176802 (2014).

[53] W. Li, J. Carrete, N. A. Katcho, and N. Mingo, Shengbte: A solver of the boltzmann transport equation for phonons, Comput. Phys. Commun. **185**, 1747 (2014).

[54] I. Romanovsky, C. Yannouleas, and U. Landman, Patterns of the Aharonov-Bohm oscillations in graphene nanorings, Phys. Rev. B **85**, 165434 (2012).

[55] H. Li, Y. Wang, X. Kang, S. Liu, and R. Li, Enhancement of thermoelectric properties in benzene molecule junction by the magnetic flux, J. Appl. Phys. **121**, 065105 (2017).